A Wireless, Low-Power, and Miniaturized EIT System for Remote and Long-Term Monitoring of Lung Ventilation in the Isolation Ward of ICU

Lin Yang, Meng Dai, Hang Wang, Xinsheng Cao, Shiqin Li, Feng Fu, Junying Xia, and Zhanqi Zhao

Abstract—Individualized lung-protective ventilation strategy is essential for patients with COVID-19. In this study, a wireless, low-power, and miniaturized electrical impedance tomography (EIT) system was developed for remote and long-term monitoring of lung ventilation for patients with COVID-19 in the isolation ward of ICU. A new strategy of combining filtering and improved voltage-controlled current was employed to design the current source for a simplified system structure, and a new differential receiver circuit consisting of a buffer amplification and a differential amplification was proposed to design the voltage measurement unit for high precision. Moreover, a Bluetooth interface was adopted for wireless data transmission, and components characterized by low power consumption were selected to minimize the system power consumption. The proposed EIT system occupies a total size of $6.5 \times 4.5 \times 0.6$ cm^3 and can work stably within 25 m from the wireless terminal installed with host EIT software. The system has a signal-to-noise of 70 dB at 50 kHz, stability of 0.1% relative change, and power consumption of 114 mW, as tested with a resistor phantom. Furthermore, a comparison between the proposed system and a commercial ICU EIT device was conducted on nine healthy volunteers for ventilation monitoring. The correlation between lung volume and relative impedance changes was higher than 0.9 for both EIT systems ($p < 0.001$). The analysis of the corresponding EIT images revealed that both systems delivered comparable images in terms of linearity, repeatability, and regional ventilation distribution. The test and experimental results suggested that the proposed system could conveniently provide reliable data acquisition (DAQ) for remote and long-term lung ventilation monitoring.

Index Terms—Electrical impedance system, low power, lung ventilation monitoring, miniaturization, wireless transmission.

Lin Yang, Hang Wang, and Xinsheng Cao are with the Department of Aerospace Medicine, Fourth Military Medical University, Xi'an 710032, China.

Meng Dai and Feng Fu are with the Department of Biomedical Engineering, Fourth Military Medical University, Xi'an 710032, China (e-mail: fengfu@fmmu.edu.cn).

Shiqin Li is with the School of Preclinical Medicine, Fourth Military Medical University, Xi'an 710032, China.

Junying Xia is with Shanghai Hynitron Technology Company Ltd., Xi'an 710065, China (e-mail: shcnxjy@163.com).

Zhanqi Zhao is with the Department of Biomedical Engineering, Fourth Military Medical University, Xi'an 710032, China, and also with the Institute of Technical Medicine, Furtwangen University, 78054 Villingen-Schwenningen, Germany (e-mail: zhanqi.zhao@hs-furtwangen.de).

I. INTRODUCTION

A NOVEL coronavirus disease (COVID-19) has been rapidly spreading worldwide since the end of 2019, resulting in a global pandemic. For those severe patients admitted to intensive care units, ventilation support is highly required but the mortality rate remains very high, ranging from 20 to 80% [1]. One potential reason is that general lung-protective ventilation strategies (e.g., low tidal volume, high positive end-expiratory pressure) maybe not enough to minimize ventilator-induced lung injury [2]. Thus, individualized ventilation strategies are essential for lung protection [3]–[5]. Unfortunately, few techniques are available for real-time monitoring and understanding of the respiratory system [6]–[8].

Electrical impedance tomography (EIT) is a non-invasive and radiation-free clinical imaging technique, which has been widely used to monitor ventilation distribution in real time and at the bedside [9]–[11]. Although computerized tomography (CT) outperforms EIT in terms of spatial resolution, EIT has substantially better temporal resolution [12]; namely, it can provide 100 frames of impedance image per second at most [13]. EIT has been applied to guide ventilation strategies, such as lung recruitment [14] and titration [15]. Also, with the ability of real-time imaging, EIT provides unique information on lung ventilation and perfusion for COVID-19 patients [16], [17]. Nevertheless, specialized designs of EIT for COVID-19 in the isolation ward of ICU might be essential.

1) COVID-19 is a highly contagious type of pneumonia [18] posing high risk of infection to medical staff, especially those who handle patients with severe COVID-19. Therefore, it is utterly necessary to propose a novel design of wireless data transmission for EIT so that medical staff can reduce the chance of contact with COVID-19 patients and thus the risk of infection.

2) As it is reported that mechanical ventilation for severe COVID-19 patients lasts for approximately 14 days on average [19], the proposed EIT is expected to perform continuous monitoring of mechanically ventilated patients. Therefore, it is preferable to choose battery power to reduce ac interference and utilize low-power chips to maximize its working duration.

3) For practical reasons in ICU, severe COVID-19 patients are often connected to various monitoring devices, treatment equipment, and isolation apparatus, etc. There might be no room at the bedside for a "bulk" EIT device similar to current commercial equipment. Consequently, it is necessary to design a wireless, low-power, and miniaturized EIT system for remote and long-term monitoring of lung ventilation in the isolation ward of the ICU.

To date, several groups have developed their wireless and portable EIT systems (Table I). In 2008, Yue and McLeod [20] designed an field programmable gate array (FPGA)-based wireless EIT system named OXBACT-5 for thoracic imaging. However, the large dimension (75 × 55 × 30 cm^3) and high power consumption (12.3 W) of the system may not allow for convenient and long-term use, and its performance test of human imaging was not illustrated. In 2015, Huang and Loh [21] created a portable EIT system named data acquisition (DAQ) based on the carbon nanotube for real-time spatial sensing, but they did not detail the system's performance. In the same year, Hong et al. [22] proposed a low power consumption EIT system-on-chip, but the system transmitted data through a USB cable rather than a wireless manner, excluding its use in the isolation ward of the ICU. In 2016, Huang et al. [23] developed a wearable and wireless EIT system by microminiaturizing the conventional EIT system and achieved in vivo imaging, but the performance of this system was not reported. In 2019, Singh et al. [24] established a low-cost portable wireless EIT system using Raspberry Pi. However, they did not show the results of human respiratory imaging, and the power consumption might be relatively high with Raspberry Pi taking into account. Moreover, some research groups also realized novel wearable systems for specific thorax EIT applications such as 3-D imaging and monitoring of patients with chronic lung diseases [25], [26]. In brief, these systems achieved expected results in preliminary experiments, nevertheless, they could not be directly used for remote and long-term monitoring of lung ventilation for COVID-19 patients. First, these EIT systems were not validated by being compared with commercially available devices in terms of imaging performance on humans. Second, none of the above systems evaluated long-term stability, which is of critical importance for long-term monitoring of lung ventilation. Third, key performance parameters of these systems, such as power consumption, signal-to-noise ratio (SNR), volume, and wireless data transmission, need to be further improved.

In this study, we proposed a wireless, low-power, and miniaturized EIT system, which could be connected to an Android tablet or a personal computer via Bluetooth. The performance of the whole system was assessed on a high-precision resistor phantom. Furthermore, the imaging performance of the proposed EIT system was evaluated on healthy volunteers and compared with that of a commercially available product, PulmoVista 500 (Draeger Medical, Luebeck, Germany).

II. MATERIALS AND METHODS

A. Overall Architecture of EIT System Design

The basic framework of the proposed wireless, low-power, and miniaturized EIT system is shown in Fig. 1(a). It mainly consisted of three parts: the conductive rubber electrode belt, the EIT DAQ module, and the Android tablet or personal computer as a host. Technically, the electrode belt consisting of 16 electrodes was attached to the thorax surface to inject steady and safe currents into s subject's thorax and collect boundary voltages simultaneously. The EIT DAQ module was designed to provide a low power current source, as well as to measure, amplify, and demodulate boundary voltage. The ∼30 mW low-power solution of AD5933 providing up to 100 kHz impedance measurements [27] is not suitable for our applications since extra power is required to measure impedance between 100 Ω and 1 kΩ which needs extra circuits attached to the chip. In the entire process of boundary voltage acquisition, a 32 bit, ultralow-power advanced RISC (reduced instruction set computer) machine (ARM) chip STM32L431CBU6 (STMicroelectronics N.V., Geneva, Switzerland) was adopted as the microcontroller unit (MCU) to achieve accurate control of the excitation and measurement circuit as well as demodulation. Subsequently, the demodulated boundary voltage was transmitted to an Android tablet or personal computer via a Bluetooth module. Finally, a series of dynamic impedance images were reconstructed in the tablet or PC with a dedicated EIT software.

Additionally, in order to minimize the system volume, the entire hardware system was powered by a small lithium battery. Therein, the current source module, the voltmeter module, the time sequence design, and the imaging algorithm comprised the critical elements of the whole system. A detailed illustration of the proposed EIT system design is given in Fig. 1(b).

B. Low Power Current Source

A direct digital synthesizer (DDS) is usually employed to generate excitation signals for impedance measurements. However, the power consumption of the DDS, either implemented by a single DDS chip or the FPGA, is a concern in a low-power solution. Here, we directly filtered a square signal generated from MCU to save power at the cost of inflexible frequency setting due to the fixed parameters of the filter. The current source was designed using a new strategy of combining filtering and voltage-controlled current with the aim of simplifying system structure and reducing the power consumption of the system. The block diagram of the current source circuit of the EIT system is shown in Fig. 2. It primarily contained an amplitude-and-frequency-adjustable square wave signal generator, a bandpass filter (BPF), and a voltage-controlled current source (VCCS).

The square wave generating circuit with adjustable amplitude and frequency consisted of a high-precision digital-to-analog converter (DAC), an analog switch, and an MCU.

TABLE I
PERFORMANCE COMPARISON OF THE PROPOSED EIT SYSTEM VERSUS OTHER TYPICAL PORTABLE SYSTEM

	The proposed EIT system	EIT DAQ system	EIT SoC system	Microminiaturizing EIT system	OXBACT-5 EIT system	WMFEIT system
Application	Lung ventilation monitoring	Spatial structural sensing	Lung ventilation monitoring	Lung ventilation monitoring	Thoracic imaging	clinical imaging
SNR	70 dB	-	56.3 dB	-	73.9 dB for real component and 66 dB for imaginary component	70 dB
Consistency error	0.46%	-	-	-	-	0.7%
Long-term stability	0.1% for 3 hours	-	-	-	-	-
ADC resolution (bit)	14	24	10	12	14	10
Frame rate	20	-	20	-	25	70
Power consumption	114 mW	-	10.4 mW	650 mW	12.3 W	10 mW
Host system	Developed based on Android and Windows	Developed based on LABVIEW	Developed based on Android	Developed based on C#	Developed based on QNX	Developed based on Matlab
Frequency (kHz)	50	-	10,50,100,200	10-200	1-100	1-1000
Channels	16	16	32	16	16 excitation current channels and 64 voltage measurement channels	16
Power supply	Battery	Power line	USB-OTG cable	Mobile power	Battery/ USB 2.0 connections	Battery
Transmission interface	Wireless Bluetooth	10/100base-t Ethernet LAN	USB-OTG cable	Wireless Bluetooth v2.0+EDR	Wireless LAN 802.11b interface	Raspberry pi 2
Reconstruction algorithm	GREIT	Maximum a Posteriori	Newton-Raphson	Back-projection	-	-
Human experiment	Yes	-	Yes	Yes	No	No
Dimension (L*W*H)	6.5*4.5*0.6 cm^3	Two-layer printed circuit board	860*40*2 mm^3	7.5*7*2 cm^3	-	5*3*2 cm^3

-denotes not mentioned.

The high-precision DAC produced a stable voltage signal with adjustable amplitude, which, together with the ground level signal, was sent to the input terminals of the analog switch. The control terminal of the analog switch was driven by a high-frequency clock provided by the MCU so that a square wave signal with adjustable amplitude and frequency could be generated as the output terminal of the analog switch. In theory, a square wave signal contained the components of a fundamental frequency signal and its high-order odd harmonics. Next, the square wave signal passed through a BPF which could filter out higher harmonics to obtain a sine signal. An operational amplifier with low power consumption, LTC6256 (Analog Devices Inc., USA), was employed to design a third-order Butterworth BPF by connecting a first-order *RC* filter circuit to the front end of the classic second-order Butterworth active BPF. The first-order *RC* filter circuit could improve the roll-off characteristics of the BPF without unduly increasing the power consumption of the system. Additionally, the center frequency of the BPF could be changed by adjusting the digital potentiometers, thereby achieving a controllable frequency and amplitude of the sine signal by the MCU.

The VCCS was designed to have a differential output. Its positive output terminal contained a Howland current pump, ensuring high output impedance. At its negative terminal, an inverting amplifier was added to the standard Howland current pump. Because the inverting amplifier could adjust the voltage on the other end of the load, the desired electric
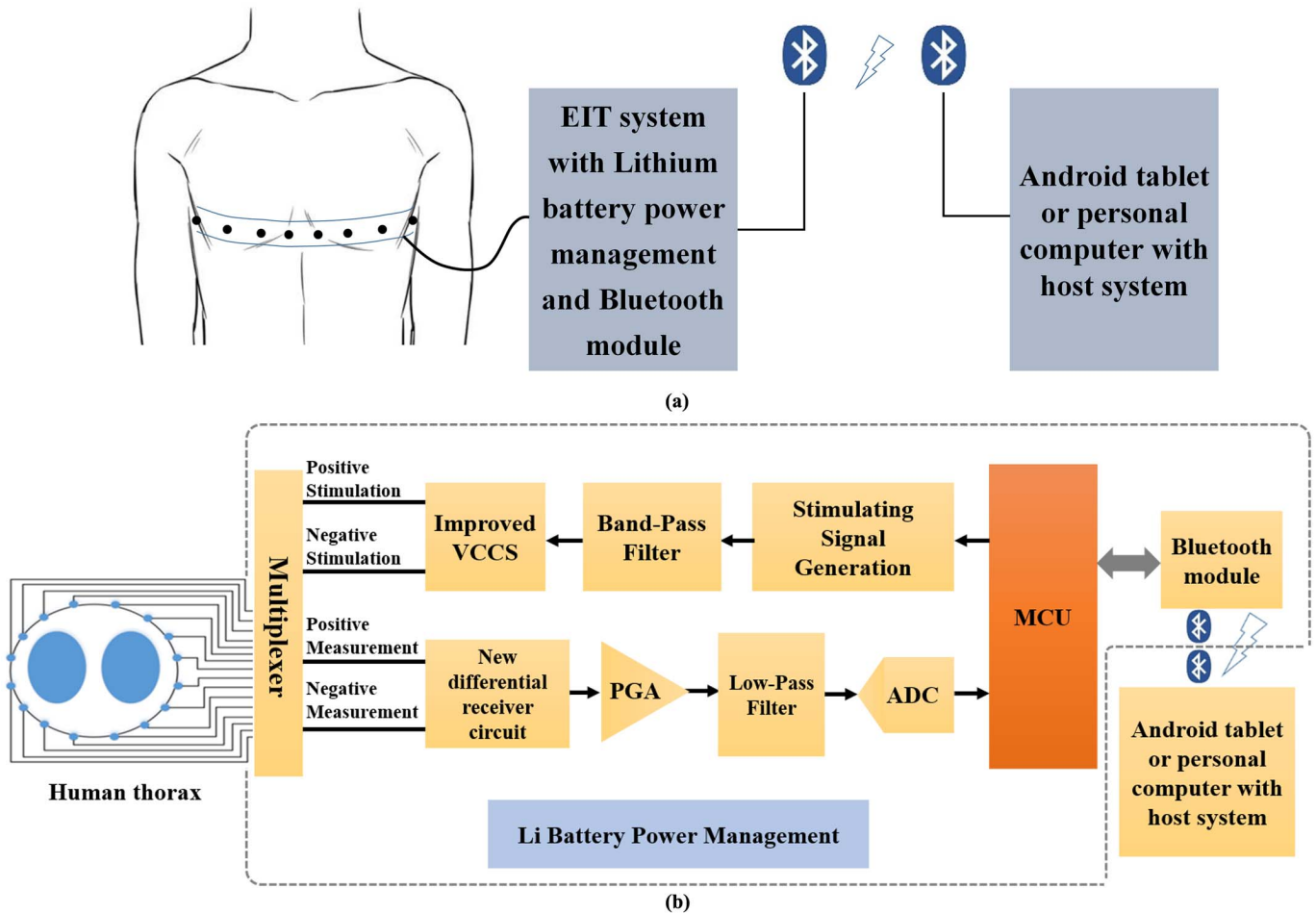
Fig. 1. Overall architecture of EIT system design. (a) Basic framework of the proposed portable and wireless EIT system. (b) Detailed block diagram.
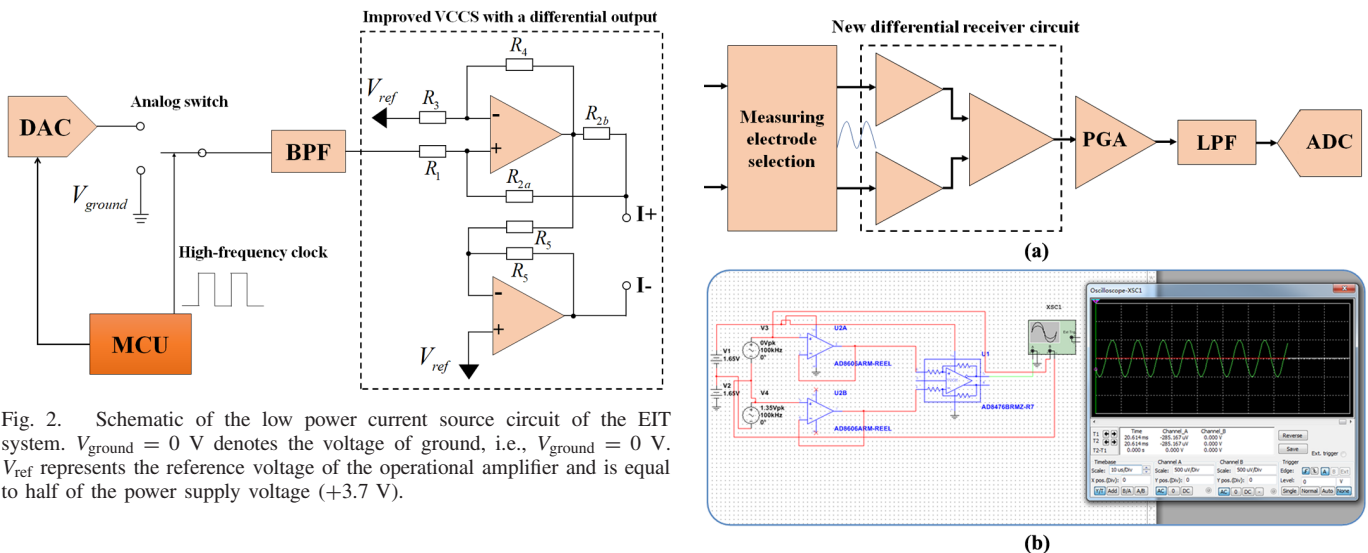

Fig. 2. Schematic of the low power current source circuit of the EIT system. $V_{\text{ground}} = 0$ V denotes the voltage of ground, i.e., $V_{\text{ground}} = 0$ V. V_{ref} represents the reference voltage of the operational amplifier and is equal to half of the power supply voltage (+3.7 V).

Fig. 3. Voltage measurement unit. (a) Schematic of the voltage measurement circuit of the EIT system. (b) Simulation results of the differential receiver circuit at 50 kHz.

current with the desired amplitude was able to pass the load. Therefore, the differential voltage on the load could reach approximately twice the value compared with that generated by the standard Howland current pump, which meant that the dynamic range of the stimulating signal was extended. The actual test showed that the output range of the current source was 100–750 μA.

C. Voltage Measurement Unit

The current excitation of a sine wave signal was applied to the thorax through a pair of electrodes selected by the

stimulating electrode selection circuit, and a response volt-age signal was then measurable on the thorax surface. The measuring electrode selection circuit allocated a pair of electrodes for voltage signal acquisition, and the acquired voltage signal was buffered and amplified by a differential receiver circuit. Considering the existence of relatively high common-mode voltages between two measurement electrodes caused by electrode-skin contact impedance, a differential receiver circuit was required, which ought to have excellent capabilities of common-model rejection, high precision, low noise, as well as wide dynamic range. Therefore, a differential receiver circuit consisting of a buffer amplifier and a differential amplifier was proposed, as shown in Fig. 3(a). We adopted two low-power input–output operational amplifiers LTC6262 (Analog Devices Inc., USA) with high precision in the buffer amplification circuit to ensure high input impedance of the differential receiver circuit, which would prevent the conversion of common-mode signals into differential-mode signals. Also, a fully differentially precision amplifier AD8476 (Analog Devices Inc., USA) with very low power and an integrated gain resistor for unity gain was adopted to complete the reception of the differential measurement signal. The sum of supply current of the three amplifiers was only 810 μA (240 μA for LTC6262 and 330 μA for AD8476), which guaranteed low power consumption. At the same time, the simulation results showed that the common-mode rejection ratio (CMRR) of the differential receiver circuit we designed was better than 70 dB at 50 kHz [Fig. 3(b)].

Subsequently, the voltage signal entered a programmable gain amplifier (PGA) circuit and was further amplified to suitable amplitude because the voltage signal collected in the actual EIT DAQ was very weak. The PGA was realized by replacing the feedback resistor of the inverting amplifier with a digital potentiometer (TPL0501). Because the operational amplifier LTC6256 (Analog Devices Inc., USA) only consumed 65 μA with a wide bandwidth of 6.5 MHz, this simple PGA structure could provide desirable programmable gain performance and keep low power consumption at the same time. Next, a fourth low-pass active filter with a stopband boundary frequency of 150 kHz was designed to perform low pass filtering for the amplified signal, so that high-frequency harmonics and noise could be prevented from entering the sampling result of the backend through aliasing.

Finally, a 14 bit, low-power, high-speed analog-to-digital conversion (ADC) chip ADS7057 (Texas Instruments Inc., USA) with a maximum sampling rate of 2.5 MSPS was selected to convert the processed response voltage signal into a digital signal. The converted signal was then demodulated to extract electrical impedance information in the MCU by using the orthogonal sequential digital demodulation method, whose effectiveness has been validated in suppressing random noise and interference in the signal as well as accurately extracting impedance signals [28], [29]. The specific demodulation process was as follows.

During the acquisition of the response voltage signal, the voltage signal was continuously sampled at equal intervals (T/N), where T was the period of the stimulating signal. Subsequently, for each period, we could obtain a data
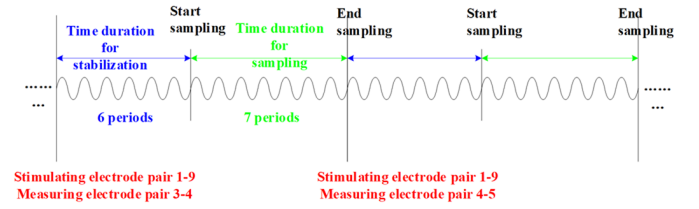

Fig. 4. Time sequence diagram of sampling for two cycles.

sequence $V_s(k)$ with N points, wherein $k = 0, 1, 2, \ldots, N - 1$. In the frequency domain, the square wave signal was a weighted superposition of the sinusoidal signal with the same frequency and its odd harmonic signal was: $V_s(t) = (4A_m/\pi) \sum_{n=1}^{\infty} (\sin((2n - 1)\omega t))/(2n - 1)$, where A_m was the amplitude of the square wave. If we constructed an in-phase component sequence $S_I(k) = \sin((2\pi k)/N)$, $(k = 0, 1, \ldots, N - 1)$ and an orthogonal component sequence $S_Q(k) = \cos((2\pi k)/N)$, $(k = 0, 1, \ldots, N - 1)$, the in-phase component I and the orthogonal component Q of the voltage sequence could be obtained by the dot product of the two sequences with the response voltage signal sequence, respectively

$$I = \sum_{i=0}^{N-1} S_I(k) \cdot V_s(k) = \frac{N}{2} A \sin\left(\phi + \frac{\pi}{N}\right) \tag{1}$$

$$Q = \sum_{i=0}^{N-1} S_Q(k) \cdot V_s(k) = \frac{N}{2} A \cos\left(\phi + \frac{\pi}{N}\right) \tag{2}$$

where $A = 4(A_m/\pi)$ was the amplitude of the fundamental sine component and ϕ was the additional phase. Next, the amplitude of the fundamental sine component, which included the impedance information of the thorax, could be obtained by demodulation $A = (2/N)(I^2 + Q^2)^{1/2}$.

D. Time Sequence Design for Data Sampling

In this study, we fixed the frequency of the stimulating signal at 50 kHz. For one measurement using the protocol of opposite stimulation-adjacent measurement (e.g., stimulating electrode pair 1–9 and measuring electrode pair 3–4, as shown in Fig. 4), we obtained a 13-period signal, with six periods for stabilizing the signal and seven periods for sampling the signal. In each period of the signal, there were 22 sampling points. Therefore, $13 \times (1/50000) = 0.26$ ms was required for one measurement. For one frame of EIT data containing 192 measurements, 0.26*192 = 49.92 ms was needed.

E. Other Auxiliary Circuits and Host System

The Bluetooth wireless interface was employed for wireless communication between the host computer and the circuit board. In the EIT system, a wireless communication circuit was designed based on an ultralow-power consumption Bluetooth System-on-Chip CC2541 (Texas Instruments Inc., USA) with a high transmission speed of up to 2 Mb/s, which satisfied the requirement of transmitting demodulated EIT voltage signals. The actual test showed that the stable transmission distance was within 25 m under barrier-free

conditions. Additionally, in order to minimize power consumption, the entire hardware system was powered by a small-size ($3 \times 1 \times 0.15$ cm^3) lithium battery (capacity: 240 mAh) which could provide a +3.7 V power supply. Moreover, a power switch was used to turn the power on or off and the lithium battery could be charged when the USB port on the circuit board was powered on.

In this study, two EIT system programs were developed to be installed on a tablet with the Android operating system and a personal computer with the Windows operating system. The programs could receive the demodulated boundary voltage transmitted by the wireless communication circuit, and reconstruct real-time EIT images as well as control the parameter configuration of the EIT acquisition system, such as the amplitude of the excitation current. In the two EIT system programs, the multi-threaded approach was adopted, and DAQ and image reconstruction were executed in different threads.

F. EIT Reconstruction Algorithm

This study employed the Graz consensus reconstruction algorithm for EIT (GREIT) algorithm developed for lung EIT imaging [29]. First, a finite element model of a male thorax was established based on a real chest CT image, including the thoracic contour and the two lung contours [31]. The thorax model consisted of 10 171 triangular elements in total. The 16 simulated electrodes with 1 cm diameter were located on the surface of the thorax, reflecting an actual EIT measurement setup. The stimulation pattern was set to "opposite stimulation-adjacent measurement" corresponding to the protocol of stimulation-measurement used by our EIT system.

GREIT algorithm aims to obtain an optimal linear reconstruction matrix $\mathbf{R}$ by minimizing the following error e^2 using a set of "training targets" for a predefined "noise figure." noise figure" is used to measure the extent to which random measurement noise is amplified in the reconstructed images and it is set by the weighting matrix [30]

$$e^2 = \sum_k \left\| \boldsymbol{\sigma}^{(k)} - \mathbf{R}\mathbf{v}^{(k)} \right\|_{\mathbf{W}}^2 \tag{3}$$

where k represents the number of all training measurement and noise samples, $\boldsymbol{\sigma}$ denotes the desired EIT image, $\mathbf{v}$ denotes the boundary voltages of the "training target," and $\mathbf{W}$ is a weighting matrix that represents the weight of each target in the training target set. In this article, we predefined "noise figure" at 0.5 to calculate the reconstruction matrix $\mathbf{R}$ (1024×192 matrix, where 1024 denotes the image size (32×32) and 192 denotes the measurements of one frame of data) in advance for image reconstruction.

III. RESULTS

The proposed system occupies a small size ($6.5 \times 4.5 \times 0.6$ cm^3). The frame rate of the entire system can be up to 20 f/s. The actual test showed that our system could drive and measure a load resistor of about 5 kΩ (4.98 kΩ) without saturation when using the maximum current excitation (750 μA p–p, p–p denotes

"peak-to-peak"). In order to evaluate the performance of the proposed system, the phantom experiments on a resistor model and the human lung imaging experiments on healthy volunteers were performed.

A. System Performance on the Resistor Model

We implemented the system performance test on a dedicated resistor model consisting of 32 100 Ω resistors with a precision of 0.1%, whose topological structure is shown in Fig. 5(a). The proposed EIT system was connected to the resistor model and continuously acquired EIT data using the protocol of opposite stimulation-adjacent measurement for 3 h when the output was configured to 700 μA p–p. The key performance parameters closely related to actual lung imaging were analyzed, including consistency, stability, SNR, as well as power consumption.

Consistency reflects the difference in measurement results of all channels. As one specific frame of EIT data included 192 measurements, we regrouped 192 measurements into six levels according to the location relationship between stimulating electrodes and measuring electrodes [Fig. 5(b)]. Then normalized data in each level by its average were determined. Next, the standard errors corresponding to each level were calculated. These standard errors ranged from 0 to 1. Finally, we defined the consistency by one minus the average of six standard errors. The computation can be expressed as

$$\text{Consistency} = 1 - \frac{1}{6} \sum_{n=1}^{6} \text{std}(\text{norm}(\mathbf{v}_n)) \tag{4}$$

where $\mathbf{v}_n$ denotes the nth level of measurement voltage [$n = 6$ in this study, as shown in Fig. 5(b)], norm($\cdot$) and std($\cdot$) represent the normalization and standard error, respectively. Herein, we obtained the consistency of our system as 0.9954 (1 means complete consistency and 0 means no consistency).

Stability reflects the change of measurement results of all channels over time. First, measurement results of all channels in one frame of data were summed up to obtain the total boundary voltage. Second, stability was defined as the ratio of standard error and the average for 3 h. The formulation can be expressed as

$$\text{Stablity} = \frac{\text{std}\left(\sum_m \sum_n v_{i,j}\right)}{\text{mean}\left(\sum_m \sum_n v_{i,j}\right)} \times 100\% \tag{5}$$

where $v_{i,j}$ denotes the measured voltage on the jth electrode pair when the current is injected through the ith electrode pair, n and m represent the number of channels ($n = 192$) and frames in 3 h ($m = 20 \cdot 60 \cdot 60 \cdot 3 = 216000$), respectively. The stability was found to be 0.0454%, better than 0.1% for 3 h [Fig. 5(c)].

SNR evaluates the level of noise in the measurement results, which reflects the reliability of measurement results. SNR was defined as the ratio of average and standard error for each measurement channel during 3 h, and it was shown that the SNR for 192 measurement channels was greater than 70 dB [Fig. 5(d)].

For power consumption, the consumed current was around 22.3 mA [Fig. 5(e)] when the Bluetooth and wireless acquisition were turned off, and within 27.4–31.2 mA when the
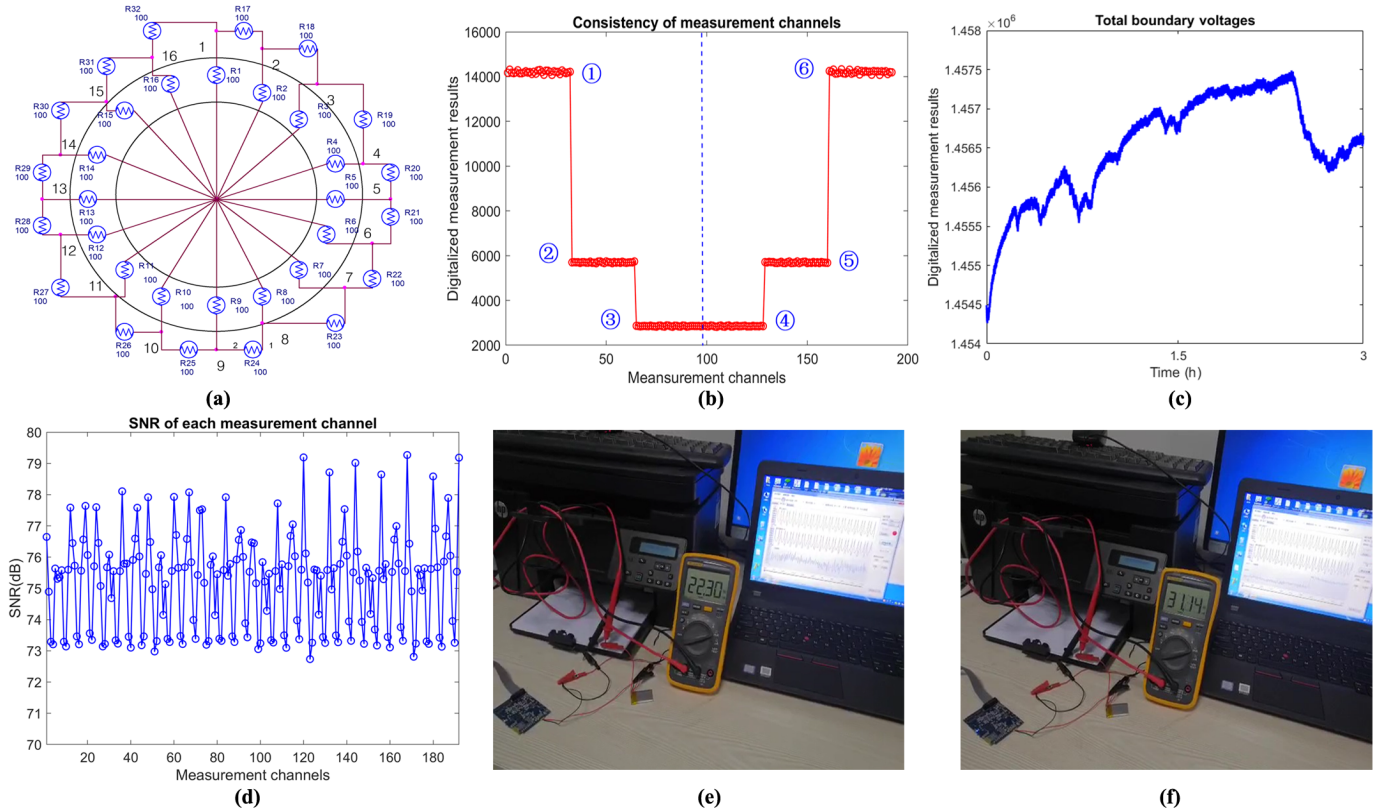
Fig. 5. Test results of system performance on the resistor model under the condition that the EIT data were continuously acquired using the protocol of opposite stimulation-adjacent measurement for 3 h when the output was configured to 700 μAp–p (p–p denotes "peak-to-peak"). (a) Topological structure of the resistor model. (b) Six levels of measurement voltage according to the location relationship between stimulating electrodes and measuring electrodes. (c) Change of measurement results of all channels over time. (d) SNR of all channels. (e) and (f) Consumed current when the Bluetooth and wireless acquisition are turned off and on, respectively.

Bluetooth and wireless acquisition were turned on [Fig. 5(f)]. As we used a lithium battery of 240 mAh in this system, theoretically, the EIT system could acquire data wirelessly for approximately 8 h.

B. System Performance on Human Lung Imaging

To further evaluate the actual measurement of the proposed portable system, an experiment was conducted on healthy lung volunteers, and the results were compared to that measured with the current commercial product, PulmoVista 500. The study protocol was approved by the ethics committees of the Fourth Military Medical University (KY202004769-5) and all subjects signed the informed consent form before the experiment. A total of nine healthy lung volunteers were prospectively examined (male; age, 34 $\pm$ 14 years; height, 172 $\pm$ 7 cm; weight, 73 $\pm$ 12 kg). The subjects were asked to perform repetitive slow vital capacity (SVC) maneuvers with a spirometer. EIT measurements were performed in the following sequence during each SVC with: 1) portable system; 2) PulmonVista500; 3) portable system; and (4) PulmonVista500. The electrode belts (Draeger, Luebeck, Germany) were attached and detached from the subjects' thorax, ~fourth intercostal space (Fig. 6). The level of the electrode plane was marked to ensure the repeatability of electrode placements for every measurement. The current of 5 mA at 50 kHz was employed in EIT measurements by

PulmonVista500 and the current of 700 μA at 50 kHz by our system. Relax stable tidal breathing and functional residual capacity level were observed before the SVC maneuver was conducted.

Tidal variation images (the difference between end-inspiration and end-expiration) were calculated. Impedance values were normalized to the corresponding SVC in milliliters. The clinically widely EIT parameters were used to evaluate the differences of the measured data [31]. To be specific, the following measures are calculated.

The (a)–(b) linearity, i.e., the ratio of the tidal variation and global impedance changes obtained during SVC (Fig. 6, TV/SVC), as well as the correlation between volume and global impedance changes in individual subjects. The global impedance value of each EIT image was obtained by computing the sum of the impedance values of all pixels in each EIT image. Linear interpolation was applied for the spirometry data to match the number of data points recorded by EIT.

The (c)–(d) global ventilation distribution, indicated by the tidal variation in the right and left lungs [Fig. 6, $D_{\text{Right}}/(D_{\text{Right}} + D_{\text{Left}})$], as well as in the ventral and dorsal regions [$D_{\text{Ventral}}/(D_{\text{Ventral}} + D_{\text{Dorsal}})$].

The (e)–(f) regional ventilation distribution, indicated by the center of ventilation (CoV) [33], [34] and the global inhomogeneity (GI) index [32], [35]. Student T-test was used to

Variability of two repeated measurements with same devices	The proposed portable system	PulmoVista500 from Draeger
TV/SVC	14.7%	16.7%
Volume-Impedance correlation	3.4%	5.1%
Right lung to global ratio	4.7%	4.0%
Ventral to global ratio	4.9%	6.9%
CoV	1.5%	2.4%
GI	4.6%	4.2%

TV: tidal impedance variation; SVC: impedance variation during SVC maneuver; CoV: center of ventilation; GI: the global inhomogeneity index.
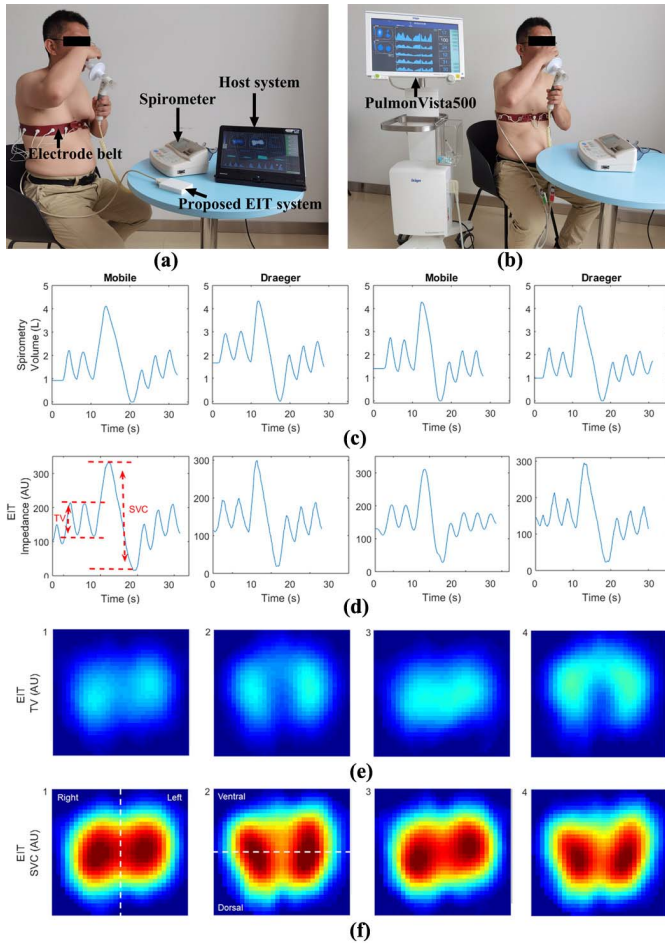
Fig. 6. View of human lung imaging and illustration of measurement sequence as well as relative impedance changes. (a) Experiment with the proposed system. (b) Experiment with the current commercial product, Pulmo-Vista 500 (Draeger Medical, Luebeck, Germany). (c) Relax tidal breaths and SVC maneuvers recorded with a spirometer. (d) Impedance-time curves during the SVC maneuver. The impedance refers to the global impedance computed by the sum of the impedance values of all pixels in each EIT image. (e) Tidal variation images during tidal breathing. (f) Impedance variation during SVC. AU: arbitrary unit.

compare the differences of EIT measures between two devices. Bland–Altman plots were used to illustrate the differences. Differences between two measurements from the same devices were divided by the average to show the repeatability of the maneuver. The value $p < 0.05$ was considered statistically significant.

The evaluated EIT parameters calculated based on the EIT data from our system and PulmoVista500 were similar, as illustrated in Fig. 7. No statistical significance was found in the parameters ($p > 0.05$). The repeatability (variability) of measures from the same device is summarized in Table II.

IV. DISCUSSION

An EIT system that could perform remote and long-term monitoring of pulmonary function is highly required for individualized lung-protective ventilation strategies for patients with COVID-19 in the isolation ward of ICU. Based on this new clinical requirement, a newly designed, wireless, low-power, and miniaturized EIT system was proposed in this study. Results showed that our system had an excellent SNR

(70 dB), superior stability (0.1% within 3 h), and a high frame rate (20 f/s). The advantages of wireless data transmission (25 m), small size ($6.5 \times 4.5 \times 0.6$ cm^3), and low power consumption (114 mW) allowed for remote and long-term monitoring of lung ventilation. Also, the host systems based on tablets and PC further facilitated the clinical application.

In order to dynamically monitor respiratory ventilation in real time, fast sampling is one of the indispensable requirements. On the one hand, a microcontroller, ARM chip STM32L431CBU6 operating at a frequency of up to 80 MHz, was used as MCU to perform time sequence logical control on sampling data of the ADC, ensuring that the signal acquisition was completed in a short time. On the other hand, the data demodulation was performed in the MCU, rather than in the host computer, because the raw response voltage signal obtained by sampling significantly increased the real-time processing burden if it was directly transmitted to the host computer. Finally, the sampling time for one frame of data was less than 50 ms and the acquisition frame rate of our system could be up to 20 f/s.

High precision is another critical requirement that ensures the accuracy of imaging results. In the current source, we designed a differential output, in which the classical standard Howland current source structure and an inverting amplifier structure were employed as the positive and negative output to ensure the high output impedance and the wide range of output current. The experimental results on the resistor model showed that the change of output current was less than 0.1% for 3 h. In the voltage measurement unit, we proposed a novel differential receiver circuit consisting of a buffer amplification and a differential amplification to improve the CMRR of the differential receiver circuit (CMRR > 70 dB at 50 kHz). Additionally, in data demodulation, the orthogonal sequential digital demodulation method was applied to suppress random noise and interference in the acquired voltage signal while the averaged results of sampled values at the same relative position in multiple cycles were demodulated to further improve the demodulation accuracy. The practical test on the resistor network showed that the SNR of the entire system was greater than 70 dB.

For the requirement of wireless transmission, the Bluetooth interface with a high transmission speed was utilized to transmit the demodulated signal to the host computer. Actual test results showed that the frame loss rate of Bluetooth transmission for EIT measurement was less than 0.1%, manifesting
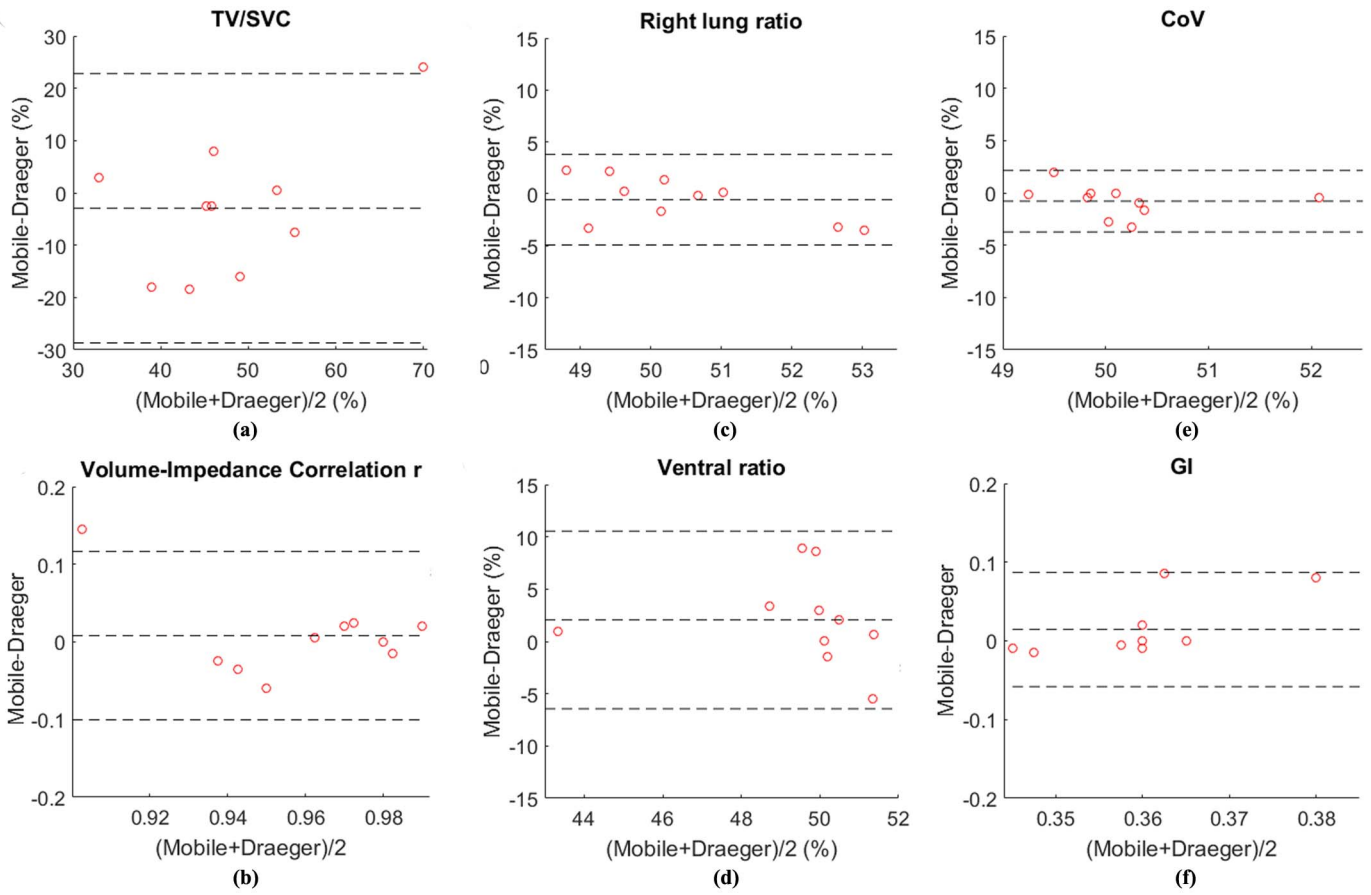
Fig. 7. Bland–Altman plots compared the EIT-based measures calculated with our proposed system (portable) and the PulmoVista500 (Draeger). (a) TV/SVC. (b) Volume–impedance correlation. (c) Right lung ratio. (d) Ventral ratio. (e) CoV. (f) GI. TV: tidal impedance variation. SVC: impedance variation during SVC maneuver.

the reliability of Bluetooth transmission. Additionally, in order to minimize the volume of the system for convenient use in the isolation ward of ICU, we employed several innovative methods as follows. First, for the current source, a new strategy of combining filtering and the voltage-controlled current was adopted instead of the classic programmable current source which consisted of a control and interface module, a programmable clock generator, a memory unit, an address generator, a DAC, a low-pass smoothing filter, and a VCCS [28]. Second, for the data demodulation, the orthogonal sequential digital demodulation method carried out in the MCU was used instead of designing a demodulation circuit [36]. Third, for hardware system power, a small-size ($3 \times 1 \times 0.15$ cm^3) lithium battery (capacity: 240 mAh) was utilized instead of developing a power module circuit [21] or using a power line/USB cable [23].

Furthermore, to minimize the system power consumption for long-term monitoring of lung ventilation, on the one hand, the entire hardware system was powered with a low-voltage single power supply. On the other hand, all components used in our system had the characteristic of low power consumption, including the ultralow-power ARM chip as MCU, the low-power input–output operational amplifier LTC6262 as the buffer amplification, the ultralow-power, fully differentially precision amplifier AD8476 as the differential measurement and the ultralow power consumption Bluetooth system-on-chip

CC2541 as transmission interface. Performance results showed that the entire hardware system consumed only 114 mW.

In the human imaging experiments, we established a finite element model of a male thorax based on a real chest CT image. It was used for image reconstructions of all the subjects in order to compare the performance of our system and the commercial product. Due to the absence of an individualized thorax model for each subject, model errors were inevitable in the reconstructed images [37]. However, for each subject in this study, the same model was used for EIT image reconstruct, rendering the model errors uniform for each subject's reconstructed EIT images. Statistically, the model errors would not affect the comparison results of reconstructed images of both the EIT systems. Consequently, the comparison of imaging performance between the two EIT systems was reliable concerning the human imaging experiments in this study.

In this study, to evaluate the imaging performance of our EIT system, we conducted a comparison between the proposed system and PulmoVista 500 on nine healthy volunteers for ventilation monitoring, in which the electrode belt of PulmoVista 500 was used for both systems. The use of the same electrode belt was intended to ensure that the results came only from the difference of the hardware systems, thus reflecting the imaging performance of the two systems. For future electrode application in clinical practice, we have conceived

three solutions. First, considering the desirable performance and wide use of ECG electrodes [38]–[40], we plan to use them connected to our hardware system through an electrode wire with concealed buttons. However, the shape of the ECG electrode will be customized to an oval shape for convenient placement on the chest. Second, to achieve rapid attachment of the electrodes, a disposable electrode belt with 16 built-in ECG electrodes is considered. Third, given the wide use of the conductive rubber electrode belt of PulmoVista 500, we plan to design a new conductive rubber electrode belt with medical gel on both sides of the electrode belt, which could be more suitable for our system in terms of the shape, conductivity (determined by the content of conductive carbon black), and fixedness. In the future, we will choose an optimal electrode solution by comparing the performances of these three solutions in terms of convenience and conductivity (including contact impedance, SNR, and long-term stability), etc.

As a limitation of this study, the number of subjects recruited in the validation experiment is limited and all volunteers were male college students who have similar demographics. The experiment was carried out in only one body position. Nevertheless, the comparison of our system with a widely used commercial product (PulmoVista 500) indicated that the performance of our system was comparable to PulmoVista 500 in terms of image analysis and interpretation. The performance of the proposed system should be further validated in clinical environmental settings. Additionally, the EIT system reported in this article needs to be further optimized. The output current of the current source can be increased for further improved SNR by optimizing the design of the current source and adopting components with better performance. An increase of 12 dB SNR may be gained when the output current is set to 3 mA, which is below the safe current limitation of 5 mA for patients defined by IEC60601-1-1 [41].

V. Conclusion

To meet the new clinical requirement of remote and long-term monitoring of lung ventilation for patients with COVID-19 in the isolation ward of ICU, a wireless, low-power, and miniaturized EIT system was developed in this study. In the design of the current source and voltage measurement unit, new strategies were adopted to ensure miniaturization and high precision, including combining filtering and improved voltage-controlled current as well as the use of a new differential receiver, which consisted of a buffer amplification and a differential amplification. Moreover, the Bluetooth interface was employed for wireless data transmission, and components characterized by low power consumption were selected to minimize the system power consumption. The overall system performance was evaluated on the resistor model in terms of consistency, stability, SNR, as well as power consumption. The actual imaging results of the system on healthy volunteers were compared with those of the existing commercial product in terms of linearity, repeatability, and regional ventilation distribution. The test and experimental results suggested that the novel EIT system could conveniently provide reliable DAQ in remote and long-term monitoring of lung ventilation.

References

[1] Z. J. Lim *et al.*, "Case fatality rates for patients with COVID-19 requiring invasive mechanical ventilation. A meta-analysis," *Amer. J. Respiratory Crit. Care Med.*, vol. 203, no. 1, pp. 54–66, Jan. 2021.

[2] V. K. Gupta, B. M. Alkandari, W. Mohammed, A. M. Tobar, and M. A. Abdelmohsen, "Ventilator associated lung injury in severe COVID-19 pneumonia patients—Case reports: Ventilator associated lung injury in COVID-19," *Eur. J. Radiol. Open*, vol. 8, Jan. 2021, Art. no. 100310.

[3] A. M. Dondorp, M. Hayat, D. Aryal, A. Beane, and M. J. Schultz, "Respiratory support in COVID-19 patients, with a focus on resource-limited settings," *Amer. J. Tropical Med. Hygiene*, vol. 102, no. 6, pp. 1191–1197, Jun. 2020.

[4] S. Hoegl and B. Zwissler, "Preventing ventilator-induced lung injury—What does the evidence say?" *J. Thoracic Disease*, vol. 9, pp. 2259–2263, Aug. 2017.

[5] Z. Zhao *et al.*, "The use of electrical impedance tomography for individualized ventilation strategy in COVID-19: A case report," *BMC Pulmonary Med.*, vol. 21, no. 1, p. 38, Jan. 2021.

[6] L. Sang *et al.*, "Lung recruitment, individualized PEEP, and prone position ventilation for COVID-19-associated severe ARDS: A single center observational study," *Frontiers Med.*, vol. 7, Jan. 2021, Art. no. 603943.

[7] F. Perier *et al.*, "Electrical impedance tomography to titrate positive end-expiratory pressure in COVID-19 acute respiratory distress syndrome," *Crit. Care*, vol. 24, no. 1, p. 678, Dec. 2020.

[8] G. Hahn *et al.*, "Monitoring lung impedance changes during long-term ventilator-induced lung injury ventilation using electrical impedance tomography," *Physiological Meas.*, vol. 41, no. 9, Oct. 2020, Art. no. 095011.

[9] L. Lasarow, B. Vogt, Z. Zhao, L. Balke, N. Weiler, and I. Frerichs, "Regional lung function measures determined by electrical impedance tomography during repetitive ventilation manoeuvres in patients with COPD," *Physiological Meas.*, vol. 42, no. 1, Feb. 2021, Art. no. 015008.

[10] L. Sang, Z. Zhao, Z. Lin, X. Liu, N. Zhong, and Y. Li, "A narrative review of electrical impedance tomography in lung diseases with flow limitation and hyperinflation: Methodologies and applications," *Ann. Transl. Med.*, vol. 8, p. 1688, Dec. 2020.

[11] V. Spatenkova, E. Teschner, and J. Jedlicka, "Evaluation of regional ventilation by electric impedance tomography during percutaneous dilatational tracheostomy in neurocritical care: A pilot study," *BMC Neurol.*, vol. 20, no. 1, p. 374, Oct. 2020.

[12] A. Adler and A. Boyle, "Electrical impedance tomography: Tissue properties to image measures," *IEEE Trans. Biomed. Eng.*, vol. 64, no. 11, pp. 2494–2504, Nov. 2017.

[13] S. Khan, P. Manwaring, A. Borsic, and R. Halter, "FPGA-based voltage and current dual drive system for high frame rate electrical impedance tomography," *IEEE Trans. Med. Imag.*, vol. 34, no. 4, pp. 888–901, Apr. 2015.

[14] L. Yun, H.-W. He, K. Möller, I. Frerichs, D. Liu, and Z. Zhao, "Assessment of lung recruitment by electrical impedance tomography and oxygenation in ARDS patients," *Medicine*, vol. 95, no. 22, p. e3820, May 2016.

[15] H.-J. Hsu *et al.*, "Positive end-expiratory pressure titration with electrical impedance tomography and pressure–volume curve: A randomized trial in moderate to severe ARDS," *Physiological Meas.*, vol. 42, no. 1, Feb. 2021, Art. no. 014002.

[16] F. Zarantonello, G. Andreatta, N. Sella, and P. Navalesi, "Prone position and lung ventilation and perfusion matching in acute respiratory failure due to COVID-19," *Amer. J. Respiratory Crit. Care Med.*, vol. 202, no. 2, pp. 278–279, Jul. 2020.

[17] B. Safaee Fakhr *et al.*, "Bedside monitoring of lung perfusion by electrical impedance tomography in the time of COVID-19," *Brit. J. Anaesthesia*, vol. 125, no. 5, pp. e434–e436, Nov. 2020.

[18] K. A. Walsh *et al.*, "SARS-CoV-2 detection, viral load and infectivity over the course of an infection," *J. Infection*, vol. 81, no. 3, pp. 357–371, Sep. 2020.

[19] M. Krause, D. J. Douin, T. T. Tran, A. Fernandez-Bustamante, M. Aftab, and K. Bartels, "Association between procalcitonin levels and duration of mechanical ventilation in COVID-19 patients," *PLoS ONE*, vol. 15, no. 9, Sep. 2020, Art. no. e0239174.

[20] X. Yue and C. McLeod, "FPGA design and implementation for EIT data acquisition," *Physiol. Meas.*, vol. 29, pp. 1233–1246, Oct. 2008.

[21] S.-K. Huang and K. J. Loh, "Development of a portable electrical impedance tomography data acquisition system for near-real-time spatial sensing," *Proc. SPIE*, vol. 9435, Apr. 2015, Art. no. 94350E.

[22] S. Hong, J. Lee, J. Bae, and H.-J. Yoo, "A 10.4 mW electrical impedance tomography SoC for portable real-time lung ventilation monitoring system," *IEEE J. Solid-State Circuits*, vol. 50, no. 11, pp. 2501–2512, Nov. 2015.

[23] J.-J. Huang, Y.-H. Hung, J.-J. Wang, and B.-S. Lin, "Design of wearable and wireless electrical impedance tomography system," *Measurement*, vol. 78, pp. 9–17, Jan. 2016.

[24] G. Singh, S. Anand, B. Lall, A. Srivastava, and V. Singh, "A low-cost portable wireless multi-frequency electrical impedance tomography system," *Arabian J. Sci. Eng.*, vol. 44, no. 3, pp. 2305–2320, Mar. 2019.

[25] M. Kim *et al.*, "A 1.4-m Ω-sensitivity 94-dB dynamic-range electrical impedance tomography SoC and 48-channel hub-SoC for 3-D lung ventilation monitoring system," *IEEE J. Solid-State Circuits*, vol. 52, pp. 2829–2842, Nov. 2017.

[26] E. Kaimakamis *et al.*, "Applying translational medicine by using the WELCOME remote monitoring system on patients with COPD and comorbidities," in *Proc. IEEE EMBS Int. Conf. Biomed. Health Informat. (BHI)*, May 2019, pp. 1–4.

[27] A. Hafid, S. Benouar, M. Kedir-Talha, F. Abtahi, M. Attari, and F. Seoane, "Full impedance cardiography measurement device using raspberry PI3 and system-on-chip biomedical instrumentation solutions," *IEEE J. Biomed. Health Informat.*, vol. 22, no. 6, pp. 1883–1894, Nov. 2018.

[28] W. Li *et al.*, "Fast high-precision electrical impedance tomography system for real-time perfusion imaging," *IEEE Access*, vol. 7, pp. 61570–61580, 2019.

[29] X. Shi *et al.*, "Design and implementation of a high-precision electrical impedance tomography data acquisition system for brain imaging," in *Proc. IEEE Biomed. Circuits Syst. Conf. (BioCAS)*, Oct. 2016, pp. 9–15.

[30] A. Adler *et al.*, "GREIT: A unified approach to 2D linear EIT reconstruction of lung images," *Physiological Meas.*, vol. 30, no. 6, pp. S35–S55, Jun. 2009.

[31] L. Yang *et al.*, "Lung regions identified with CT improve the value of global inhomogeneity index measured with electrical impedance tomography," *Quant. Imag. Med. Surg.*, vol. 11, no. 4, pp. 1209–1219, Apr. 2021.

[32] Z. Zhao, I. Frerichs, S. Pulletz, U. Muller-Lisse, and K. Moller, "The influence of image reconstruction algorithms on linear thorax EIT image analysis of ventilation," *Physiol. Meas.*, vol. 35, pp. 1083–1093, Jun. 2014.

[33] I. Frerichs, P. A. Dargaville, H. van Genderingen, D. R. Morel, and P. C. Rimensberger, "Lung volume recruitment after surfactant administration modifies spatial distribution of ventilation," *Amer. J. Respiratory Crit. Care Med.*, vol. 174, pp. 772–779, Oct. 2006.

[34] I. Frerichs, G. Hahn, W. Golisch, M. Kurpitz, H. Burchardi, and G. Hellige, "Monitoring perioperative changes in distribution of pulmonary ventilation by functional electrical impedance tomography," *Acta Anaesthesiol. Scandinavica*, vol. 42, pp. 721–726, Jul. 1998.

[35] Z. Zhao, K. Möller, D. Steinmann, I. Frerichs, and J. Guttmann, "Evaluation of an electrical impedance tomography-based global inhomogeneity index for pulmonary ventilation distribution," *Intensive Care Med.*, vol. 35, no. 11, pp. 1900–1906, Nov. 2009.

[36] X. Shi *et al.*, "High-precision electrical impedance tomography data acquisition system for brain imaging," *IEEE Sensors J.*, vol. 18, no. 14, pp. 5974–5984, Jul. 2018.

[37] B. Grychtol, W. R. Lionheart, M. Bodenstein, G. K. Wolf, and A. Adler, "Impact of model shape mismatch on reconstruction quality in electrical impedance tomography," *IEEE Trans. Med. Imag.*, vol. 31, no. 9, pp. 1754–1760, Sep. 2012.

[38] S. Leonhardt and B. Lachmann, "Electrical impedance tomography: The holy grail of ventilation and perfusion monitoring?" *Intensive Care Med.*, vol. 38, pp. 1917–1929, Dec. 2012.

[39] I. Frerichs *et al.*, "Chest electrical impedance tomography examination, data analysis, terminology, clinical use and recommendations: Consensus statement of the translational EIT development study group," *Thorax*, vol. 72, no. 1, pp. 83–93, Jan. 2017.

[40] C. Putensen, B. Hentze, S. Muenster, and T. Muders, "Electrical impedance tomography for cardio-pulmonary monitoring," *J. Clin. Med.*, vol. 8, no. 8, p. 1176, Aug. 2019.

[41] *Medical Electrical Equipment—Part 1–1: General Requirements for Safety—Collateral Standard: Safety Requirements for Medical Electrical Systems*, Standard IEC 60601-1-1, International Electrotechnical Commission, 2000, p. 66.
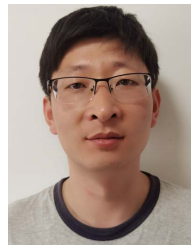
Lin Yang received the M.Sc. and Ph.D. degrees in biomedical engineering from Fourth Military Medical University, Xi'an, China, in 2014 and 2017, respectively.

He is currently a Lecturer in aerospace medicine and engineering with Fourth Military Medical University. His current research interests include medical instrumentation design, electrical impedance tomography, and image reconstruction.

Meng Dai received the M.Sc. and Ph.D. degrees in biomedical engineering from Fourth Military Medical University, Xi'an, China, in 2009 and 2012, respectively.

He is currently an Associate Professor in biomedical engineering at Fourth Military Medical University. His current research interests mainly focus on thoracic electrical impedance tomography, including data preprocessing, image reconstruction, and clinical interpretation.

Hang Wang received the M.Sc. degree in biomedical engineering and the Ph.D. degree in biophysics from Fourth Military Medical University, Xi'an, China, in 2012 and 2015, respectively.

He is currently a Lecturer in aerospace medicine and engineering at Air Force Medical University, Xi'an. His current research interests include biological tissue dielectric properties and aerospace ergonomics.

Xinsheng Cao received the M.Sc. and Ph.D. degrees in aerospace medicine from Fourth Military Medical University, Xi'an, China, in 2000 and 2004, respectively.

He is currently a Professor in aerospace medicine at Fourth Military Medical University. His current research interests include the effects of aviation acceleration on physiology and aviation ergonomics.

Shiqin Li is currently pursuing the B.S. degree in aerospace medicine with Fourth Military Medical University, Xi'an, China.

His current research interests include electrical impedance tomography and aerospace medicine.

Feng Fu received the B.S., M.S., and M.D. degrees in biomedical engineering from Fourth Military Medical University, Xi'an, China, in 1993, 1996, and 1999, respectively.

He is currently a Professor at the Department of Biomedical Engineering, Fourth Military Medical University. His current research interest includes bio-impedance measurement and imaging.

Junying Xia received the M.Sc. and Ph.D. degrees in instrument science and technology from the National University of Defense Technology, Changsha, China, in 2014 and 2017, respectively.

He was involved in hardware system and image reconstruction algorithm on electrical impedance tomography, from 2013 to 2020. Since 2021, he has been a Senior Algorithm Engineer with Shanghai Hynitron Technology Company Ltd., Xi'an China. His current research interests include electrical impedance tomography, algorithms related to fingerprint recognition, and image processing.

Zhanqi Zhao was born in Guangzhou, China, in November 1982. He received the M.Sc. degree in biomedical engineering from Furtwangen University, Villingen-Schwenningen, Germany, in 2008, and the Ph.D. degree in human biology from Ludwig Maximilians University of Munich, Munich, Germany, in 2013.

Since 2008, he has been working on the optimization of mechanical ventilation and clinical applications of electrical impedance tomography (EIT). Since 2015, he has been leading the clinical research of chest EIT in the Chinese community and involved in more than 90% of the relevant clinical studies in China. He is currently affiliated with Fourth Military Medical University, Xi'an, China, and Furtwangen University.

Dr. Zhao is a member of the International EIT Steering Committee and serves for the moment as a Consultant for Dräger Medical and eResearchTechnology, Estenfeld, Germany.